

Strides, steps and stumbles in the march of the seasons

Brian E. Mapes¹, Nikolaus Buenning¹, In-Sik Kang², George N. Kiladis³, David M. Schultz⁴,
Klaus M. Weickmann¹

¹*NOAA/CIRES Climate Diagnostics Center, Boulder, Colorado*

²*Climate Environment System Research Center, Seoul National University,
Seoul, Republic of Korea*

³*NOAA Aeronomy Laboratory, Boulder, Colorado*

⁴*CIMMS, University of Oklahoma, and NOAA National Severe Storms Laboratory, Norman, Oklahoma*

Corresponding author address:

Brian Mapes, CIRES, 216 UCB, Boulder CO 80309-0216, USA, email: brian.mapes@noaa.gov

Submitted to BAMS

June 2004

ABSTRACT

The mean seasonal cycle at daily resolution is examined in multi-decade climate data sets, including global reanalyses, gridded rain gauge data, satellite products, and climate model outputs. Slow variations (with annual and semi-annual periods) are examined with sinusoidal Fourier harmonics. Higher-frequency features are detected and depicted using wavelet analysis, and are emphasized in this article. Because solar (orbital) forcing has essentially no high-frequency components, such phenomena must involve nonlinear dynamics within the Earth system. For this reason, they pose useful challenges for climate models. Seasonal phenomena shown here include: 1. The annual harmonic of near-surface temperature, which already poses a challenge for climate system models; 2. Semiannual variations of jet streams and the Northern Hemisphere mid-winter minimum of storms; 3. Summer rainy-season onsets in the monsoons; 4. Mid-summer enhancements of the oceanic subtropical highs and associated monsoon rainfall breaks; 5. Sudden onset of autumn rains in the northwest U.S.; and 6. A climatological oscillation in late northern winter associated with the long-debated ‘January thaw’ in North America.

A free software package is offered, for reproducing and extending these results. Called the Annual Cycle Explorer (ACE), the package included a graphical user interface and many datasets.

Introduction

The seasonal cycle is the heartbeat of Earth's climate, driven by the “march” of the sun back and forth across the equator. This basic solar forcing is smoothly varying in time, except near the poles where the sun disappears entirely during winter. The amplitude spectrum of top-of-atmosphere (TOA) insolation (Fig. 1) is dominated by the annual harmonic (365-day period) everywhere off the equator. The semiannual harmonic has modest amplitude in (and somewhat beyond) the Tropics, where the sun passes overhead twice a year, and considerable amplitude at high latitudes, where it and other even harmonics are required to fully represent the flat-bottomed sunless or “coreless” winter (van Loon 1967).

This insolation forcing evokes complex, nonlinearly interacting responses in many components of the Earth system, including the atmosphere, land surface, cryosphere, upper oceans, and biosphere (including human activities). As a result, the concept of the seasons encompasses a wide range of phenomena, from simple “strides” like the almost sinusoidal variation of surface temperature in middle latitudes (e.g. Trenberth 1983), through subtler seasonal “steps” like monsoon onsets, to mysterious “stumbles,” sometimes called *singularities* (Glickman 2000) or *calendricities* (Brier et al. 1963), like the long-debated North American ‘January Thaw’, at the edge of statistical significance (Godfrey et al. 2002).

Human interest in the seasons is far older than science, so this study needs little in the way of motivation. Local lore about calendrical weather events exists in many parts of the world. Between this lore and the published weather and climate literature, including a large body of historically interesting older work (reviewed in Talman, 1919 for example), there are plenty of hypotheses to examine and phenomena to try to understand. As computers, analysis methods,

models and data sets have grown in sophistication, the annual cycle seems due for a modern scientific revisitation. Today it is possible to assemble a global observational picture of the seasonal cycle, with more than 20 years of data available even for hard-to-estimate variables like precipitation over oceans. The mean annual cycle provides a graded set of tests for climate models, with some heartening successes already, but also some robustly observed phenomena that pose a worthy challenge.

This paper describes a small sample of results from our ongoing study of the seasonal cycle at daily resolution. We have conducted a standardized Fourier and wavelet analyses of about a million 365-day time series, representing the climatology of many variables at many geographical locations in many datasets. This analysis (described in more detail below) yields a set of spectral coefficients describing the cycles and events in the seasonal march. This set of coefficients serves as a useful index to the variations contained in the full set of daily data values, but is an additional large data set in its own right. To access all these data effectively, we developed a graphical user interface (GUI) program called the Annual Cycle Explorer (ACE). A modestly-sized (600 MB) version of ACE is free to obtain and run through our Web site <http://www.cdc.noaa.gov/people/nik.buenning/ACE.html>. The examples presented here and several others are illustrated on the Web site, and are easily reproduced as a starting point for further explorations by calling them from a menu of pre-defined settings for ACE.

Time series analysis method

To illustrate our basic Fourier and wavelet analysis, Fig. 2 shows an example: the 27-year mean (1968-1996) time series of daily-mean surface air temperature at the 42.5N, 102.5W grid-point (western Nebraska) in the NCEP/NCAR reanalysis (Kalnay et al. 1996; it should be noted

that surface temperature is a fairly model-dependent field in reanalysis, as assimilation of surface data is problematic especially where smoothed model terrain height differs from station heights). A large annual cycle is evident, high in summer and low in winter (blue curve in panel a). Since the annual harmonic is directly forced, it has a large amplitude. We describe it by its phase and amplitude, and subtract it from the time series before further analysis, leaving the residual green curve in Fig. 2. A small semiannual harmonic (183d period) is evident, responsible for the relatively cool temperatures in late spring (May-June) seen in the full time series, characteristic of the western United States and Europe which lie on the cool side of spring-enhanced subtropical jet streams. Since the semiannual harmonic has some direct solar forcing, and since it has little of the time localization which motivates the use of wavelet analysis, we next subtract it to yield the high-frequency (HF) residual shown in the red curve.

Because climatological HF fluctuations do not have periodic forcing through the year, they tend to have small amplitudes, and typically are not sustained oscillations. Rather, most resemble isolated event-like features, typically with single sidelobes arising from the spectral decomposition process. In addition, much of the remnant HF variability seen in the red curve on Fig. 2 is not truly climatological, but rather is simply ‘weather noise’, i.e. sampling error associated with the finite number of years entering the mean time series. Wavelet analysis (Torrence and Compo 1996, hereafter TC96) is ideally suited for characterizing event-like or locally-wavy variability. Statistical significance tests developed by TC96 offer useful objective tools for distinguishing significant HF features of climate from weather noise.

Wavelet analysis transforms a time series into a distribution of amplitude (or its square, power) as a function of both time and frequency (here expressed as period). The numerical value

of the wavelet amplitude at a particular time and period is a projection coefficient measuring the similarity of the time series around that time to a normalized wavelet basis function with wiggles of that period. (Actual computation of the wavelet spectrum is more efficiently performed in spectral space as described in TC96.) The most important arbitrary choice in wavelet analysis is how many wiggles the basis function has. A function with more wiggles produces wavelet spectra with better frequency resolution, but at the cost of time resolution.

Because climatological HF features tend to be event-like, and we care more about their date than about their exact period (or characteristic time scale), we choose the complex Paul wavelet with parameter $m=4$ (see Fig. 2 of TC96), which is similar in structure to many HF features of interest. The real part of the Paul wavelet is a symmetric peak, with one negative side-lobe on each side, approximately $1/3$ the height of the central peak. Positive (negative) amplitude in the real component of the Paul wavelet spectrum thus corresponds to maxima (minima) in the HF time series (Fig. 2c). The imaginary component of the Paul wavelet is antisymmetric, so that the imaginary wavelet amplitude depicts rises or falls in the HF time series, depending on its sign (Fig. 2d). The complex wavelet power is the sum of the squares of these components, so it is less corrugated and depicts only the presence of variability, without indicating the phase or sign (Fig. 2b). Discontinuities at January 1 associated with our finite-length climatologies are negligible in all cases examined here. In leap years, we simply discard a day.

The wavelet spectra of Figure 2 have abundant structure, most of which is just weather noise as mentioned above. In order to seek potentially significant climate signals in the midst of this noise, our analysis considers the amplitude of every peak (local extremum) in the real and imaginary wavelet power spectra (Figs 2c and 2d) between 8d and 140d period. A statistical sig-

nificance is assigned to each peak, by comparing the value of wavelet power there to the power expected for a red noise process. To account for seasonality in the noise level (winter is typically noisiest), the red-noise null hypothesis is fitted using the variance and lag correlation within the 91-day HF time series segment centered on the peak being tested. A chi-squared distribution converts this peak-to-noise ratio to a significance index, as in TC96 but with 1 degree of freedom rather than 2 since real or imaginary power rather than complex power is being evaluated. The significance index (a number between 0 and 1) can be loosely interpreted as a probability that the observed spectral peak is more than just an accidental coincidence in a random red noise process. Peaks with significance index greater than 0.9, or in some cases 0.8, are deemed potentially interesting. For these features, the peak's location (calendar day and period), signed amplitude, and significance index are stored in the file of spectral coefficients that summarize each time series.

It is important to note that this spectral-peak significance test is imperfect and incomplete. Certainly it does not reflect what we would like the 'statistical significance' of a singularity to really mean: the probability that a feature in question would persist in a climatology constructed from an infinite number of years. The test also makes no reference to the spatial coherence of a time-series feature. Experience has shown that our test is very conservative for wavelet peaks of long (intraseasonal) periods, since such peaks have a hard time rising above red noise fitted from a 91-day HF time series segment containing the peak itself. In contrast, the test is clearly too lax for short-period features, such as the 10-day peak identified as having significance of .912 near 1 June in Fig. 2c (default ACE settings exclude display of peaks with periods <25 days). Despite its shortcomings, however, this significance index serves adequately for its main purpose: simply and objectively screening for relatively high-amplitude features, worthy of closer attention, in time series of many diverse types of variables, with different values (units) and noise characteristics.

Peaks with significance index exceeding 0.9 are indicated by labels on panels c and d of Fig. 2. The broad maximum of complex wavelet power (Fig. 2b) in January-February, near 30-day period, is seen in Figs. 2c, 2d to consist of a sequence of real and imaginary peaks with significances from 0.9 to 0.941, corresponding to the rises, maxima, falls, and minima in a distinctive intraseasonal wiggle in the time series. Wavelet peaks also highlight a roughly 60-day period variation in mid-late summer, with a cool phase centered on 1 August when the northern fringes of the North American summer monsoon bring enhanced cloud and rain. A positive imaginary peak near 60-day period is also seen around early November, as temperature falls less rapidly than it would in an annual+semiannual harmonic climatology. Examination of time series farther north and east indicate that this is a robust aspect of North American climate, apparently involving the heat capacity of surface waters before they freeze, including Hudson's Bay (~1 December freeze date) and perhaps many smaller water bodies not resolved in global reanalysis.

Data sets utilized

The Fourier and wavelet analysis described above has been applied to climatological daily time series of every variable at every grid point in many data sets. In addition to the usual mean atmospheric variables on pressure surfaces, a simple synoptic eddy activity index was constructed: a 9-day window standard deviation of meridional wind. Two-dimensional variables examined include sea-level pressure, surface (2-meter) winds and temperature, precipitation, surface fluxes, outgoing longwave radiation (OLR), precipitable water, and tropopause height.

Our largest observational data set is the NCEP/NCAR reanalysis (Kalnay et al. 1996), from which we took a 27-year (1969-1996) climatology, for reasons of convenient availability. Satellite-observed OLR from the interpolated dataset of Liebmann and Smith (1996) were aver-

aged over 1979-1996. A 1979-2002 climatology of the Climate Prediction Center (CPC) Merged Analysis of Precipitation (CMAP, Xie and Arkin 1997) was constructed at pentad (5-day) resolution. Another precipitation data set used here is a 50-year gridded gauge climatology (1948-1998) covering the US and Mexico, from the U.S. NOAA Climate Prediction Center (Higgins et al. 2000).

Model data examined here include daily output from the fully coupled (atmosphere, ocean, land, and sea ice) National Center for Atmospheric Research (NCAR) Climate System Model (CSM) version 1.3, averaged over an 1870-1996 integration with time-dependent atmospheric sulfur and greenhouse gases setting the calendar (experiment code b018.15). Twenty-year climatologies from 10 atmosphere-land models driven by climatological sea surface conditions (Kang et al. 2003) are also included in ACE.

The seasonal march's great “strides”: annual and semiannual harmonics

The annual harmonic in surface air temperature (SAT) is a convenient starting point for considering the Earth's response to the annual cycle of solar radiation. Although it is strongly and directly forced by insolation, temperature is also affected by properties of the earth's surface (albedo, heat capacity, Bowen ratio) and atmosphere (cloudiness, boundary layer, winds), so already there is ample opportunity for models to differ from observations. Figure 3 shows the phase (contours and arrow direction) and amplitude (arrow length) of the annual harmonic of SAT, in reanalysis (panel a) and NCAR CSM1.3 (panel b). The largest amplitude is over the continents, especially in the northern hemisphere, with the global maximum in far eastern Siberia (> 50 K peak-to-peak in reanalysis). Over the oceans the amplitude is generally smaller, with largest values (> 10 K peak-to-peak) over the northwestern Pacific and Atlantic. The climate model

reproduces these general features fairly well, but informative differences can be seen. Over most of the oceans, the phase (expressed as a lag behind local summer solstice) is later in the model, perhaps indicating an excessive heat capacity (mixed layer depth) in the model. Over the cold tongue region of the tropical eastern Pacific, the differences are greater: observed temperature is warmest in spring, while the model ocean is warmest in summer like elsewhere on the earth. Temperatures over land in tropical monsoon regions of Asia, Australia, and central America also indicate differences. Observed temperatures lead TOA insolation by a month or two, as monsoonal rains have begun to cool the land by the time of the summer solstice., while modeled temperatures exhibit little or no such lead.

The semiannual harmonic is much less strongly forced (Fig. 1), yet is prominent in many aspects of atmospheric variability, including global atmospheric angular momentum (AAM; e.g. Huang and Sardeshmukh 2000). Upper-tropospheric winds over the tropics contribute most strongly to AAM, and have a semiannual cycle similar to that of AAM, while upper-level winds over the rest of the globe exhibit complex but systematic semiannual patterns, especially in the Pacific sector (Weickmann and Chervin 1988). For example, zonal winds at 150 hPa over the Pacific are shown in Fig. 4, as a time-latitude section. The tropical semiannual cycle is clear as an oscillation with two maxima and two minima, but other features without two peaks also involve semiannual amplitude, including the southern hemisphere subtropical and subpolar jets (cf. van Loon and Jenne 1970). The subpolar jet variation is consistent, via thermal wind considerations, with local responses to semiannual solar forcing (van Loon 1967, Meehl 1991), but the mechanism of subtropical jet variation is apparently less direct, as discussed below. In the northern hemisphere, the Pacific jet stream splits during springtime (April), with the subtropical branch persisting through spring and weakly into summer. This spring subtropical jet is important to

weather over the United States, such as the late cool springs of the west (Fig. 2) and severe storms over the Great Plains.

The north Pacific storm track also exhibits a semiannual variation, most evocatively cast as a mid-winter minimum in upper-tropospheric eddy activity (Nakamura 1992). Figure 5 displays this phenomenon as the semiannual harmonic of eddy activity (standard deviation of meridional wind in a 9-day running window) at 250 hPa. The Pacific is clearly the globe’s most prominent center, but the midwinter eddy minimum is very zonally extended, with a significant zonal-mean component. This semiannual zonal band of mid-winter eddy suppression apparently stems from some aspect of the semiannual jet-stream variations (Nakamura 1992; Harnik and Chang 2004; Newton 2004; Yin 2004). In turn, the dominant cause of these semiannual jet variations, as shown by Huang and Sardeshmukh (2000), is not a direct semiannual thermal forcing, but rather a simple advective nonlinearity arising within the annual harmonic, owing to its finite amplitude. Semiannual jet variability and Pacific-centered but zonally-extended northern winter eddy suppression are both simulated reasonably well in the CCSM climate model (not shown), supporting the idea that robust mechanisms are involved.

Seasonal “steps”: rapid rainy-season onsets

At periods shorter than semiannual, there is little direct forcing (Fig. 1), so the nonlinearities of climate dynamics must be active in setting the timing, location, and amplitude of HF climatological features. Nonlinearities include not only the dry advective dynamics of jets and eddies considered above, but also surface interactions, turbulence and convection, transport and phase changes of water, and associated radiative feedbacks. One classic example of a fast “step” in the annual march of the seasons is the onset of the summer monsoons, which involves all of these pro-

cesses acting both locally and globally (e.g. Webster et al. 1998). In this paper, we use the term *monsoon* to refer to any rainy sub-season within the astronomical summer season.

As a convenient definition of monsoon onset at each point, we can use imaginary wavelet power peaks like those indicated in Fig. 2d to assign objectively a date, significance index, and amplitude to rapid rate-of-change events. To illustrate the method in a well-documented context, Fig. 6a shows a map of onset dates of the climatological monsoon near Asia, based on the largest-amplitude wavelet-detected rapid decrease of OLR within the indicated time interval. Results compare reasonably well to other onset date maps, obtained by other methods, such as Fig. 6 of Wang and LinHo (2002), whose annotations for the Indian Summer Monsoon (ISM, Yin 1949), the East Asian Summer Monsoon (EASM, Lau and Li 1984, Tao and Chen 1987), and Western North Pacific Monsoon (WNPM, Murakami and Matsumoto 1994, Ueda et al. 1995) are reproduced on Fig. 6a. Zeng and Lu (2004) offered another definition of onset, and constructed spatial maps of its date, which also agree in general with Fig. 6a.

Earliest onset dates, in late April are seen in the western equatorial Indian ocean, peninsular Southeast Asia, extreme southeast China, and northwest Borneo. Onset over the South China Sea occurs during May, after which the mean Mei-Yu or Baiu frontal zone of the EASM marches northward toward Japan and eventually Korea. Across the Indian subcontinent, OLR-defined monsoon onset spreads gradually northward through May and June, to eventually reach the Arabian peninsula near 1 July. Meanwhile, back south in the equatorial Indian Ocean between 80E and 100E, the dominant OLR fall in the time period shown also occurs near July 1, associated with the beginnings of the second rainy phase of a climatological active-break cycle (Wang and Xu 1997). Many atmospheric and coupled climate models simulate the propagating sudden rain

onsets in the south Asian region reasonably well, but few succeed in depicting the subtler EASM onset process (Kang et al. 2003).

Wavelet depictions of the onset dates of other warm-season rainy sub-seasons (defined using OLR falls) are presented in Fig. 6. Figure 6b shows the earliest developments in the Australian monsoon, in November, the solar equivalent of May in the Northern Hemisphere. An early signal is seen impinging on northern Australia from the southwest, indicating the contribution to climatology by midlatitude frontal influences (Davidson et al. 1983), while a slightly later tropical signal is seen to move from west to east in the equatorial belt (Hendon and Liebmann 1990). A recent study of Australian monsoon onset by Hung and Yanai (2004) also implicates both midlatitude and tropical influences, although in any given year these are not necessarily both present.

Perhaps the Earth's highest-latitude summer monsoon onset (again, defined as a wavelet-detected subseasonal decrease in OLR) is the European monsoon (Roediger 1929). Figure 6c shows that a fast climatological decrease of OLR occurs on successively later dates from south to north in western Europe, and then from west to east across eastern Europe and Russia in May and early June. Rainfall data corroborate this as a rainy-season onset: for example, in a region of Russia northeast of the Black Sea, CMAP rainfall rises steeply around June 1 from its springtime climatology of about 1 mm d^{-1} to a late-June and early-July maximum more than twice as great (not shown). In association with the onset of European monsoon rains, a slight but distinct dip in the temperature curve in June is seen in long historical climatologies of surface temperature from central Europe (Floehn 1942).

In the North American sector, OLR-defined monsoon onset dates (Fig. 6d) have a large-scale similarity to those in Asia during the same range of calendar dates: a strong, sharp onset

along the semiarid southwestern margins of the continent, and a weaker SW-NE band of rainfall propagating northward off the southeast coast. The North American Monsoon (NAM) refers to the summer rains of southwestern North America (Bryson and Lowry 1955, Douglas et al. 1993, Adams and Comrie 1997, Barlow et al. 1997, Higgins et al. 1997), with clouds (low OLR, Fig. 6d) and rain (Fig.7) marching northward to reach the southwestern U.S. by early July.

A lesser-known phenomenon seen in Figs. 6d and 7 is the northward propagating late-spring (May-June) rainy season onset in the Caribbean region, reaching Florida during May (time series shown in Fig. 8a) and detectable as far as the U.S. Gulf Coast states in June. This late-spring onset of rains is well known locally in the area, but we have not encountered a name for this regional climate system in the scientific literature. One possibility is the Eastern North American Summer Monsoon (ENASM), by analogy to the EASM in Fig. 5a. In more general terms, this system is an example of a subtropical convergence zone (STCZ; Kodama 1992, 1993, 1999), which is a poleward-eastward tilting rain belt common to several western ocean basins, along the western margins of the oceanic subtropical highs.

Midsummer dry spells in the STCZs

Rainfall climatology in south Florida (Fig. 8) has spring-summer rains, whose sudden onset was depicted in Fig. 7, followed by a distinct rainfall minimum centered in late July, a part of the Caribbean - Central American midsummer drought described by Magaña et al. (1999). This hot dry midsummer sub-season is known locally (Portig 1961) in Spanish by the names *veranillo* (little summer) or *canicula* ('dog days,' named for the rising of Sirius, the dog star). Caribbean and east Pacific tropical cyclone activity is also slightly reduced in midsummer (Inoue et al. 2002, Curtis 2002). Midsummer droughts are a common feature of STCZs, as shown in the other time

series of Fig. 8. While the climatological midsummer rainfall minima are not so large in magnitude, the associated decrease in cloudiness under a summer sun causes significant rises in temperature and evaporation, contributing to true hydrological drought conditions such as crop stresses (e.g. in Japan, Asai and Fukui 1977).

The low-level flow pattern associated with the tropical Americas midsummer drought is shown in Fig. 9, as maps of sea level pressure (SLP) in early and middle summer. The Atlantic High strengthens in midsummer and protrudes westward. This causes a narrow summer peak in southern North American SLP time series in July (Fig. 10a; Bryson and Lahey 1958), in what is otherwise a season of low pressure more typical of the warmer (summer) hemisphere generally and continental longitudes in particular. A mid-summer protrusion of the western Pacific subtropical high can also be identified in association with the midsummer drought in Japan (Asai and Fukui 1977; Fig. 5 of LinHo and Wang 2002). The Asia-Pacific high pressure extension (the Ogasawara High) is overlain by an upper-level anticyclone (the Bonin High), which apparently emanates from the south Asian monsoon via equivalent-barotropic wave processes in the westerlies (Enomoto et al. 2003).

The midsummer enhancement of the Pacific High is strongest in the central basin, where it lends a distinctive strong ter-annual (~120-day period) component to the time series of pressure (Fig. 10b) and the trade winds to the south. Both the sub-seasonal mid-summer SLP maxima seen in Fig. 10, and the tropical Americas midsummer drought, are present in simulations by several atmosphere and coupled climate models (e.g. Mapes et al. 2004), suggesting that their origins may not hinge on very subtle physical processes. Presumably their origin is, like that of the seasonal mean anticyclones, a global dynamical response to land-sea heating patterns (Rodwell and

Hoskins 2001, Chen et al. 2001, Liu et al. 2004). Air-sea coupling also plays a role in the annual cycle of the anticyclones (Seager et al. 2003), but sea surface temperature varies little on the higher frequency of the midsummer enhancement. Oceanic dynamic height observations in the North Pacific show prominent sub-annual variations (Chiswell 1996), suggesting possible ocean impacts from quasi-ter-annual wind variations, but Chiswell's 3-year record (with gaps) is insufficient to indicate clearly whether their phase is tied to the calendar.

The rain-bearing weather in early vs. late summer can have different characteristics (e.g. Portig 1961). In synoptic terms, spring rains may have frontal character (as in the Mei-Yu / Baiu season in east Asia), while late-summer rain, in the Caribbean as well as east Asia, tend to come in the form of tropical disturbances or cyclones. In contrast, the South Atlantic lacks both the summer SLP peaks seen in Fig. 10 and an autumnal tropical cyclone season. Instead, there is a climatological alternation, from February to March to April, in the position of the South Atlantic Convergence Zone (SACZ; reviewed in Carvalho et al. 2004), as indicated in Fig. 11. Standing patterns are also seen in SACZ variability with time scales from submonthly to interannual (Nogués-Paegle and Mo 1997, Liebmann et al. 1999, Robertson and Mechoso 2000), supporting the idea that the underlying geography of the region may fix the structure and preferred locations of the SACZ (Figueroa et al. 1995).

The onset of autumn rains in northwestern North America

A sudden onset to rainy season is not unique to low latitudes in summer: during northern autumn, rainfall in the northwestern U.S. ramps up steeply, with a time scale faster than semian-
nual (Fig. 12a; note time axis is centered on Jan 1). Here rainfall is correlated with mean 500 hPa zonal wind (Fig. 12b), as the jet stream brings both moisture and disturbances. Although the syn-

optic noise level of this cool-season climatology is high, and the rainfall and wind data are for different epochs (1948-98 for rain vs. 1969-96 for wind), some low-frequency features are common to both time series. Complex wavelet power (contours in Fig 12c,d) has its absolute maximum centered in November, near 100-day period, in both precipitation and wind time series, corresponding to the faster-than-semiannual onset of winter. Another distinctive feature evident in both the wavelet power plots is spectral peak near 30-day period centered in early February.

A seasonal-march “stumble” in northern winter

Interestingly, the 30-day power in Fig. 12c,d coincides well in period and timing with the Nebraska temperature signal noted in Fig. 2. Observations and folklore have long hinted at climatological intraseasonal variability in winter, from the Groundhog Day legend to the long-debated January Thaw. However, the inherent variability of winter weather is so great that the possible scientific basis of such notions has remained unclear.

Writing in 1919, Charles Marvin, Chief of the Weather Bureau in the United States, considered the observations reproduced in Fig. 13a. Although he had highlighted the graphs with January-February intraseasonal anomalies (bolded curve and a and b labels), he stated that “the January Thaw, the May Freeze, etc. do not persist nor have a real existence...they are simply residual imprints of a single of a few fortuitously recurrent extreme or unusual events at or near the time in question.” Many subsequent studies have returned to this question; for a recent critical review see Godfrey et al. (2002). Much of this work has been limited to data from one or a few stations, and statistical debate on the reality or unreality of the January Thaw has typically centered on the question: *Is the mean temperature on a particular calendar day or days in late January ‘significantly’ different from ‘normal’ or ‘expected’ values* (with these terms variously

defined)? Since the magnitude of the signal in question is only a fraction of a standard deviation characterizing the day-to-day noise level of winter weather, skeptics have had no trouble defining ‘no-Thaw’ null hypotheses which observations fail to reject with statistical confidence. Without delving deeply into the debate, here we merely attempt to widen the perspective by asking a slightly different question: *Is there a climatological intraseasonal oscillation (CISO) in the Northern Hemisphere in January-February?*

Since we have seen indications of a CISO all across North America, not just in the traditional January Thaw region of New England, it makes sense to bring spatial averaging to bear on the problem of weather noise. Figure 13b shows 1969-1996 reanalysis surface temperature averaged over all of northern North America (latitudes 33-62, covering all of the northern US and southern Canada). The intraseasonal feature from Fig. 2 is now very clear, with its warm phase in late January, as in Marvin’s pre-1919 data. But is it “real”?

One plausible dynamical explanation of a winter temperature CISO might involve meridional advection by a midlatitude intraseasonal wind oscillation (Ghil and Mo 1991), arising from flow across Northern Hemisphere topography (as in Marcus et al. 1996), and hence tending to develop near a certain date in the depth of winter when the basic flow becomes unstable (as in Strong et al. 1995). The final ingredient for a CISO would be for the oscillation to tend to begin in the same phase each year, which could happen if it were a finite-amplitude instability developing from initially linear, fixed-phase mountain-induced stationary waves. A comprehensive study of this hypothesis is beyond the present scope, but the significant wavelet power peak found in these climatological data sets does serve to strongly indicate an intraseasonal spectral peak in the underlying individual-year data. The remaining observational question for whether the CISO has (in Dr.

Marvin's words) a "real existence" is whether this intraseasonal oscillation's tendency to have calendar-locked phase is statistically significant -- a question not yet addressed in the January Thaw literature.

Conclusions

The mean seasonal cycle is an old subject, with many familiar aspects but also many mysteries remaining. Seasonal-cycle observations provide an ideal set of challenges and tests for climate models, as relatively short, uninitialized model simulations can be directly compared to reliable, statistically significant features of observations. Phenomena which are reasonably well simulated by the models, but not fundamentally understood, point to tractable research challenges. Fine structure in climatology may even comprise a useful body of predictable climate variability, with genuine value in the human economy. We hope that this article, and the free ACE almanac software offered in connection with it, will open useful avenues in climate research, education, and applications.

Acknowledgements

The research published here was supported by the U.S. NOAA Office of Global Programs (OGP) Climate Prediction for the Americas Program (CPPA), and by U.S. National Science Foundation grants ATM-0112715, ATM-0097116. DMS was supported by NOAA/OAR/NSSL under NOAA/OU Cooperative Agreement NA17RJ1227.

References

- Adams, D. K. and A. C. Comrie, 1997: The North American monsoon. *Bull. Amer. Meteor. Soc.*, **78**, 2197-2213.
- Asai, T., and E. Fukui, 1977: The short dry period in mid-summer. Chapter 6 in *The climate of Japan*, Developments in Atmospheric Sciences vol. 8., Kodansha Ltd., Tokyo and Elsevier, Amsterdam, pp 103-112.
- Barlow, M., S. Nigam, and E. H. Berbery, 1998: Evolution of the North American monsoon system. *J. Clim.*, **11**, 2238-2257.
- Brier, G. W., R. Shapiro, and N. J. Macdonald, 1963: A search for rainfall calendaricities. *J. Atmos. Sci.*, **20**, 529-532.
- Bryson, R. A., and W. P. Lowry, 1955: Synoptic climatology of the Arizona summer precipitation singularity. *Bull. Amer. Meteor. Soc.*, **36**, 329-339.
- Bryson, R. A., and J. F. Lahey, 1958: *The march of the seasons*. Final report of contract AF 19-(604)-992, Department of Meteorology, University of Wisconsin, 41 pp.
- Carvalho, L. M. V., C. Jones, and B. Liebmann, 2004: The South Atlantic convergence zone: Intensity, form, persistence, and relationships with intraseasonal to interannual activity and extreme rainfall. *J. Climate*, **17**, 88-108.
- Chen, P., M. P. Hoerling, and R. M. Dole, 2001: The origin of the subtropical anticyclones. *J. Atmos. Sci.*, **58**, 1827-1835.
- Chen, P., M. P. Hoerling, and R. M. Dole, 2001: The origin of the subtropical anticyclones. *J. Atmos. Sci.*, **58**, 1827-1835.
- Chiswell, S. M., 1996: Intra-annual oscillations at station ALOHA, north of Oahu, Hawaii. *Deep Sea Res.*, **43**, 305-319.

- Curtis, S., 2002: Interannual variability of the bimodal distribution of summertime rainfall over Central America and tropical storm activity in the far-eastern Pacific. *Clim. Res.*, **22**, 141-146.
- Davidson, N.E., J.L. McBride, and B. McAvaney, 1983: The onset of the Australian monsoon during winter MONEX: Synoptic aspects. *Mon. Wea. Rev.*, **111**, 496-516.
- Douglas, M. W., R.A. Maddox, K. W. Howard, and S. Reyes, 1993: The Mexican monsoon. *J. Climate*, **6**, 1665-1677.
- Enomoto, T., B. J. Hoskins, and Y. Matsuda, 2003: The formation mechanism of the Bonin high in August. *Quart. J. Roy. Meteor. Soc.*, **129**, 157-178.
- Figueroa, S. N., P. Satyamurty, and P. L. Da Silva Dias, 1995: Simulations of the summer circulation over the South American region with an eta coordinate model. *J. Atmos. Sci.*, **52**, 1573-1584.
- Flohn, H., 1942: *Witterung und klima in Deutschland*. Verlag von S. Hirzel in Leipzig, 162pp.
- Ghil, M., and K. Mo, 1991: Intraseasonal oscillations in the global atmosphere. Part I: Northern Hemisphere and tropics. *J. Atmos. Sci.*, **48**, 752-779.
- Godfrey, C. M., D. S. Wilks, and D. M. Schultz, 2002: Is the January thaw a statistical phantom? *Bull. Amer. Meteor. Soc.*, **83**, 53-62.
- Harnik, N., and E. K. M. Chang, 2004: The effects of variations in jet width on the growth of baroclinic waves: Implications for midwinter pacific storm track variability. *J. Atmos. Sci.*, **61**, 23-40.
- Hendon, H. H., and B. Liebmann, 1990: A composite study of onset of the Australian summer monsoon. *J. Atmos. Sci.*, **47**, 2227-2240.
- Higgins, R. W., Y. Yao, and X. Wang, 1997: Influence of the North American Monsoon System on the United States summer precipitation regime. *J. Climate*, **10**, 2600-2622.
- Higgins, R. W., W. Shi, E. Yarosh and R. Joyce, 2000: Improved US precipitation quality control system and analysis. NCEP/Climate Prediction Center ATLAS No. 7, <http://www.cpc.ncep.noaa.gov/>

research_papers/ncep_cpc_atlas/7/index.html. Datasets available through www.cdc.noaa.gov

- Huang, H.-P., and P. D. Sardeshmukh, 2000: Another look at the annual and semiannual cycles of atmospheric angular momentum. *J. Climate*, **13**, 3221-3238.
- Hung, C.-W., and M. Yanai, 2004: Factors contributing to the onset of the Australian summer monsoon. *Quart. J. Roy. Meteor. Soc.*, **130**, 739 -758.
- Inoue, M., I. C. Handoh, and G. R. Bigg, 2002: Bimodal distribution of tropical cyclogenesis in the Caribbean: Characteristics and environmental factors. *J. Climate*, **15**, 2897-2905
- Kalnay, E., and Coauthors, 1996: The NCEP / NCAR 40-year reanalysis project, *Bull. Amer. Meteor. Soc.*, **77**, 437-471.
- Kang, I.-S., and 12 Coauthors, 2002: Intercomparison of the climatological variations of Asian summer monsoon precipitation simulated by 10 GCMs. *Clim. Dyn.*, **19**, 383-395.
- Kodama, Y.-M., 1992: Large-scale common features of subtropical precipitation zones (the Baiu frontal zone, the SPCZ, and the SACZ). Part I: Characteristics of subtropical frontal zones. *J. Meteor. Soc. Japan*, **70**, 813-836.
- Kodama, Y.-M., 1993: Large-scale common features of subtropical convergence zones (the Baiu frontal zone, the SPCZ, and the SACZ). Part II: Conditions of the circulations for generating the STCZs. *J. Meteor. Soc. Japan*, **71**, 581-610.
- Kodama, Y.-M., 1999: Roles of the atmospheric heat sources in maintaining the subtropical convergence zones: An aqua-planet GCM study. *J. Atmos. Sci.*, **56**, 4032-4049.
- Lau, K.-M., and M.-T. Li, 1984: The monsoon of East Asia and its global associations--A survey. *Bull. Amer. Meteor. Soc.*, **65**, 114-125.
- Liebmann, B., and C. A. Smith, 1996: Description of a complete (interpolated) outgoing longwave radiation data set. *Bull. Amer. Meteor. Soc.*, **77**, 1275-1277.

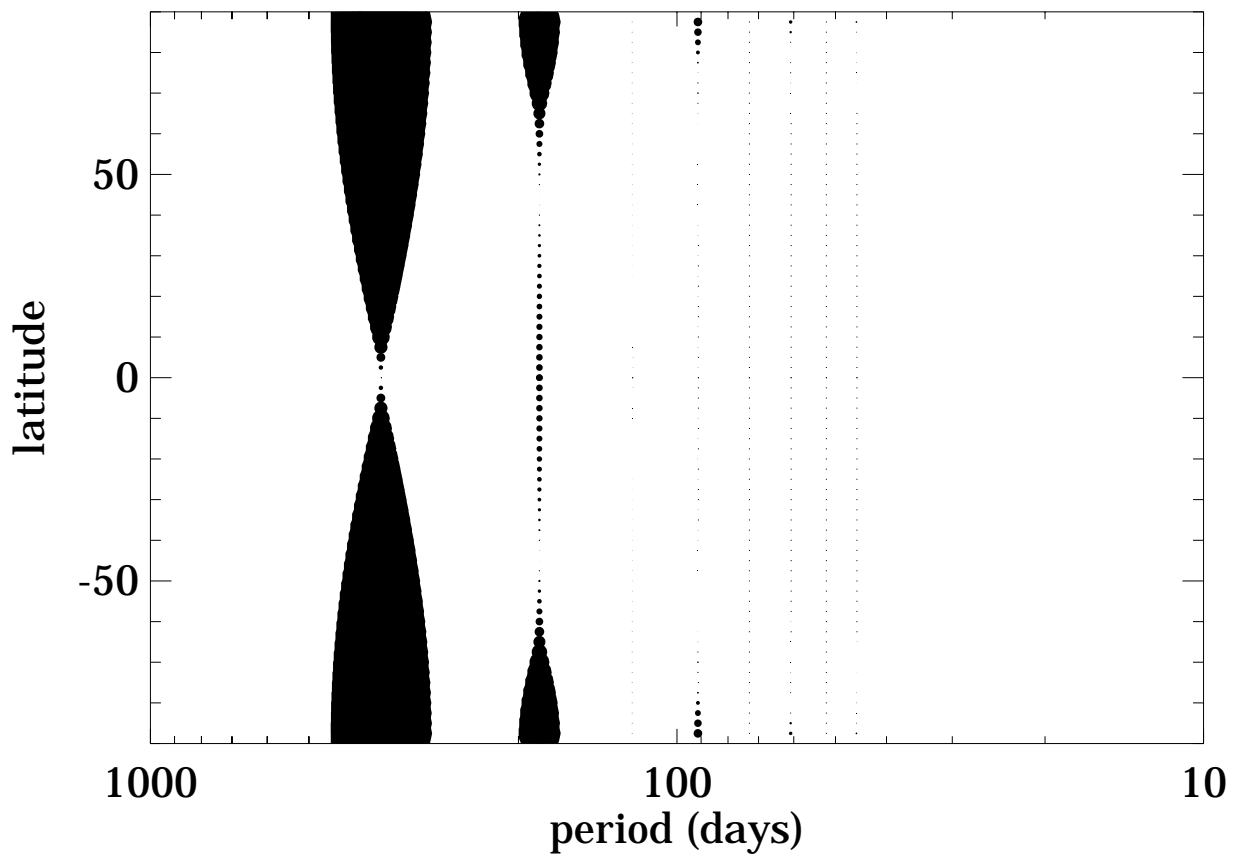
- Liebmann, B., G. N. Kiladis, J. A. Marengo, T. Ambrizzi, and J. D. Glick, 1999: Submonthly convective variability over South America and the South Atlantic convergence zone. *J. Climate.*, **12**, 1977-1991.
- LinHo and B. Wang, 2002: The time-space structure of the Asian-Pacific summer monsoon: A fast annual cycle view. *J. Climate*, **15**, 2001-2019.
- Liu, Y., G. Wu, and R. Ren, 2004: Relationship between the subtropical anticyclone and diabatic heating. *J. Climate*, **17**, 682-698.
- Magaña, V., J. A. Amador, and S. Medina, 1999: The midsummer drought over Mexico and Central America, *J. Climate*, **12**, 1577-1588.
- Mapes, B. E., P. Liu, and N. Buening, 2004b: Indian monsoon onset and Americas midsummer drought: out-of-equilibrium responses to slowly varying seasonal forcing. *J. Climate*, submitted.
- Marcus, S. L., M. Ghil, and J. O. Dickey, 1996: The extratropical 40-day oscillation in the UCLA general circulation model. Part II: Spatial structure. *J. Atmos. Sci.*, **53**, 1993-2014.
- Marvin, C.F., 1919: Normal temperatures (daily): Are irregularities in the annual march of temperature persistent? *Mon. Wea. Rev.*, **47**, 544-555.
- Meehl, G. A., 1991: A reexamination of the mechanism of the semiannual oscillation in the Southern Hemisphere. *J. Climate*, **4**, 911-926.
- Murakami, T., and J. Matsumoto, 1994: Summer monsoon over the Asian continent and western North Pacific. *J. Meteor. Soc. Japan.*, **WN**, 719-745.
- Nakamura, H., 1992: Midwinter suppression of baroclinic wave activity in the Pacific. *J. Atmos. Sci.*, **49**, 1629-1642.
- Newton, C. W., 2004: Associations between twice-yearly oscillations of the North Pacific cyclone track and upper-tropospheric circulations over the Eastern Hemisphere. *Mon. Wea. Rev.*, **132**, 348-367.
- Nogués-Paegle, J., and K. C. Mo, 1997: Alternating wet and dry conditions over South America during

- summer. *Mon. Wea. Rev.*, **125**, 279-291.
- Portig, W. H., 1961: Some climatological data of Salvador, Central America. *Weather*, **16**, 103-112.
- Robertson, A. W., and C. R. Mechoso, 2000: Interannual and interdecadal variability of the South Atlantic convergence zone. *Mon. Wea. Rev.*, **128**, 2947-2957.
- Rodwell, M. R. and Hoskins, B. J., 2001: Subtropical anticyclones and monsoons. *J. Clim.*, **14**, 3192-3211.
- Roediger, G., 1929: Der Europäische Monsun. *Veroff. Geophys. Ints. Univ. Leipzig*, **4**, 119-178.
- Seager, R., R. Murtugudde, N. Naik, A. Clement, N. Gordon, and J. Miller, 2003: Air-sea interaction and the seasonal cycle of the subtropical anticyclones. *J. Climate*, **16**, 1948-1966.
- Strong, C., F.-F. Jin, and M. Ghil, 1995: Intraseasonal oscillations in a barotropic model with annual cycle, and their predictability. *J. Atmos. Sci.*, **52**, 2627-2642.
- Talman, C.F., 1919: Literature concerning supposed recurrent irregularities in the annual march of temperature. *Mon. Wea. Rev.*, **47**, 555-565.
- Tao, S., and L. Chen, 1987: A review of recent research on the East Asian summer monsoon in China. *Monsoon Meteorology*, C.-P. Chang and T. N. Krishnamurti, Eds., Oxford University Press, 60-92.
- Torrence, C. and G. P. Compo, 1998: A practical guide to wavelet analysis. *Bull. Amer. Meteor. Soc.*, **79**, 61-78.
- Trenberth, K. E. 1983: What are the seasons? *Bull. Amer. Meteor. Soc.*, **64**, 1276-1277.
- Ueda, H., T. Yasunari, and R. Kawamura, 1995: Abrupt seasonal change of large-scale convective activity over the western Pacific in the northern summer. *J. Meteor. Soc. Japan.*, **73**, 795-809.
- van Loon, H., 1967: The half-yearly oscillations in middle and high southern latitudes and the coreless winter. *J. Atmos. Sci.*, **24**, 472-486.
- van Loon, H., and R. J. Jenne, 1969: The half-yearly oscillations in the Tropics of the Southern Hemisphere. *J. Atmos. Sci.*, **26**, 218-232.

- Webster, P. J., V. O. Magana, T. N. Palmer, J. Shukla, R. A. Tomas, M. Yanai, and T. Yasunari, 1998: Monsoons: Processes, predictability, and the prospects for prediction. *J. Geophys. Res.*, **103**, 14451-14510.
- Weickmann, K. M., and R. M. Chervin, 1988: The observed and simulated atmospheric seasonal cycle. Part I: Global wind field modes. *J. Climate*, **1**, 265-289.
- Wang, B., and X. Xu, 1997: Northern Hemisphere summer monsoon singularities and climatological intraseasonal oscillation. *J. Climate.*, **10**, 1071-1084.
- Wang, B., and LinHo, 2002: Rainy season of the Asian-Pacific summer monsoon. *J. Climate*, **15**, 386-398.
- Xie, P., and P. A. Arkin, 1997: Global Precipitation: A 17-Year monthly analysis based on gauge observations, satellite estimates, and numerical model outputs. *Bull. Amer. Meteor. Soc.*, **78**, 2539-2558.
- Yin, M. T., 1949: A synoptic-aerologic study of the onset of the summer monsoon over India and Burma. *J. Meteor.*, **6**, 393-400.
- Yin, J. H., and D. S. Battisti, 2004: Why do baroclinic waves tilt poleward with height? *J. Atmos. Sci.*, **61**, 1454-1460.
- Zeng, X., and E. Lu, 2004: Globally unified monsoon onset and retreat indices. *J. Climate*, **17**, 2241-2248

Figure captions

Figure 1: Fourier spectrum of zonal mean top-of-atmosphere incoming solar radiation, calculated for a spherical Earth in circular orbit. The size of the filled circle at each latitude and period is proportional to amplitude.



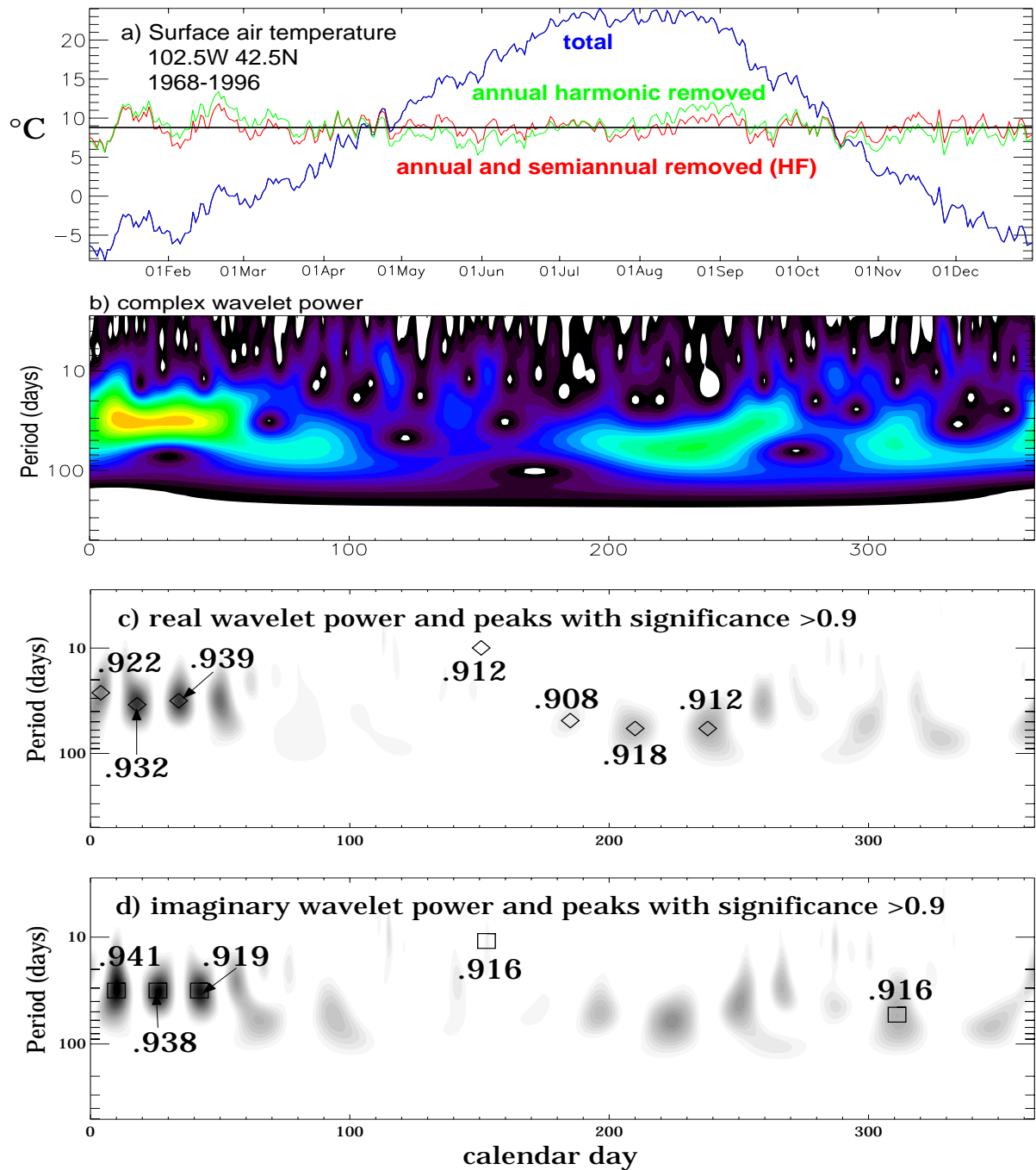


Figure 2: Example harmonic-wavelet analysis for Nebraska temperature (blue curve in a). Green curve has annual harmonic subtracted, red has semiannual subtracted as well leaving only high frequency (HF) signal. For clarity, all curves are centered on the annual mean. b) Complex wavelet power in the HF time series. Rainbow color scale shows increasing power from purple through green to orange-red. c) Real wavelet power (shading), and its peaks, which correspond to peaks and troughs in the HF time series. Only peaks with significance index >0.9 are indicated (diamonds labeled with significance index; see text). d) as in c) but for imaginary peaks, indicated by squares and corresponding to rising and falling regions in the HF time series.

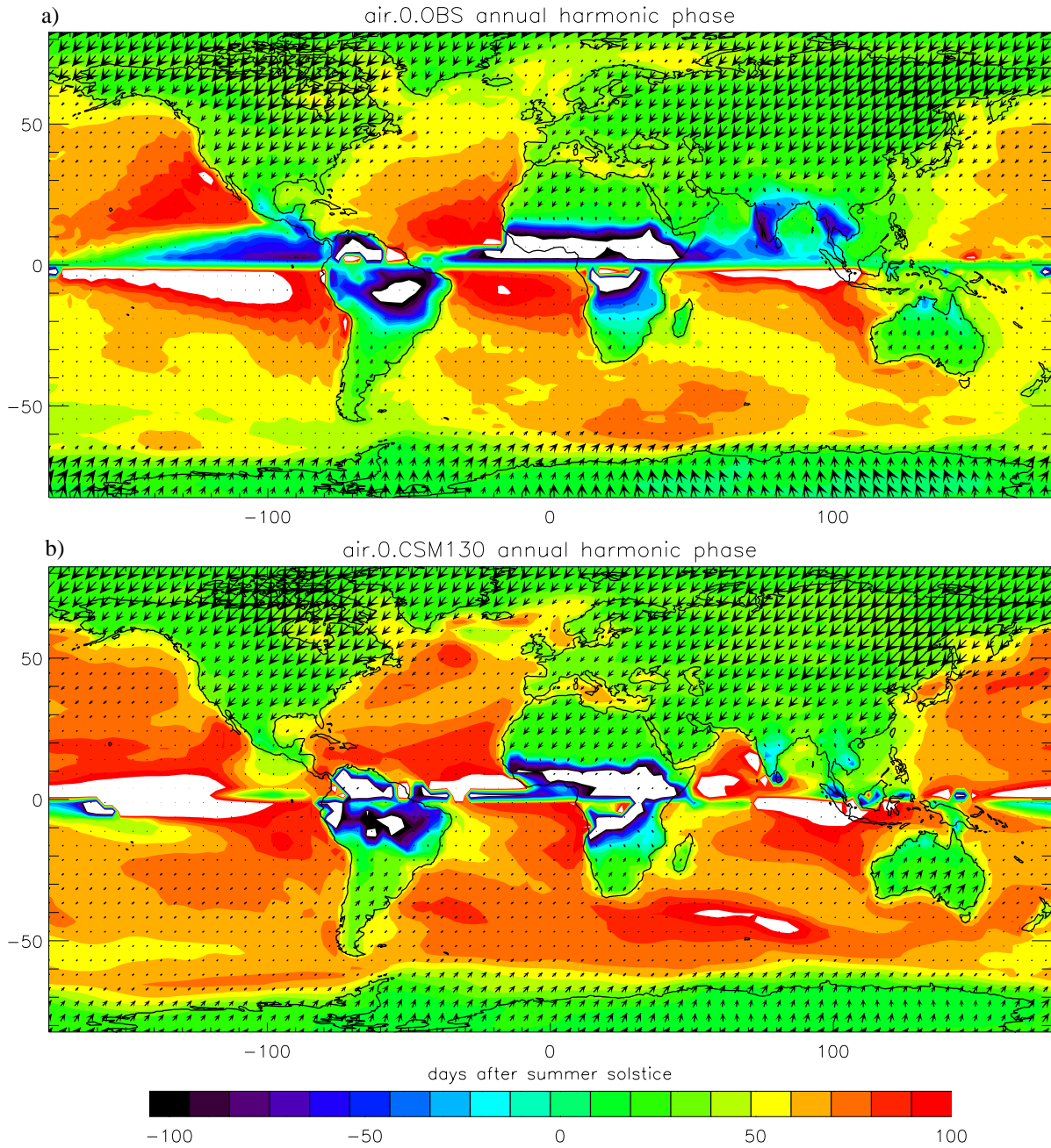


Figure 3: Annual harmonic of surface air temperature in a) NCEP reanalysis and b) the NCAR CSM 1.3 climate model. Phase is expressed by colors, as the time of the maximum value after local summer solstice (note definition is discontinuous across the equator). White areas have values beyond the ends of the indicated color table. Arrow length is proportional to amplitude, with a global maximum of 50K peak-to-peak in eastern Siberia. Arrow direction expresses phase, with northward pointing arrows indicating 1 January and eastward arrows indicating 1 April.

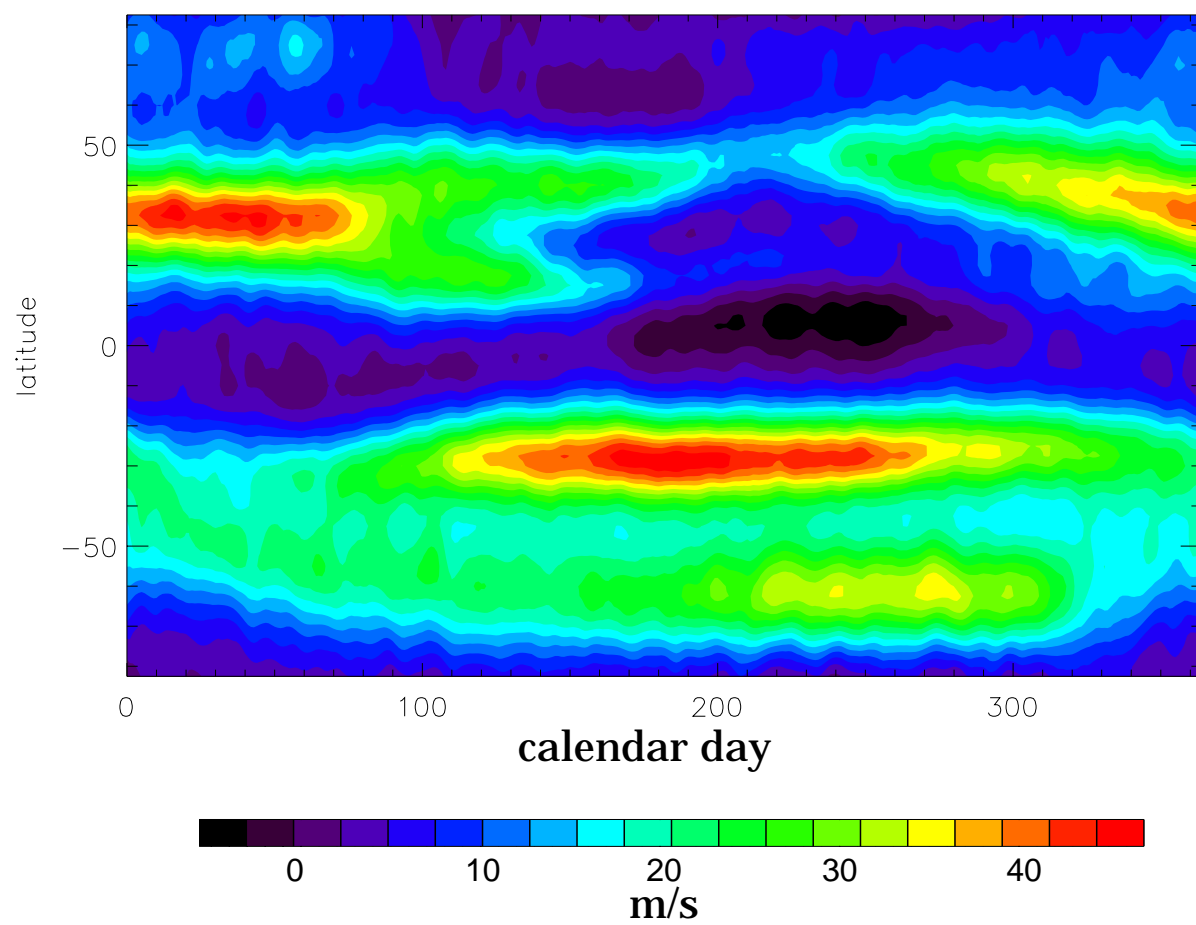


Figure 4: Time-latitude section of zonal wind at 150 hPa level over longitudes 150E - 120W (the Pacific Ocean sector).

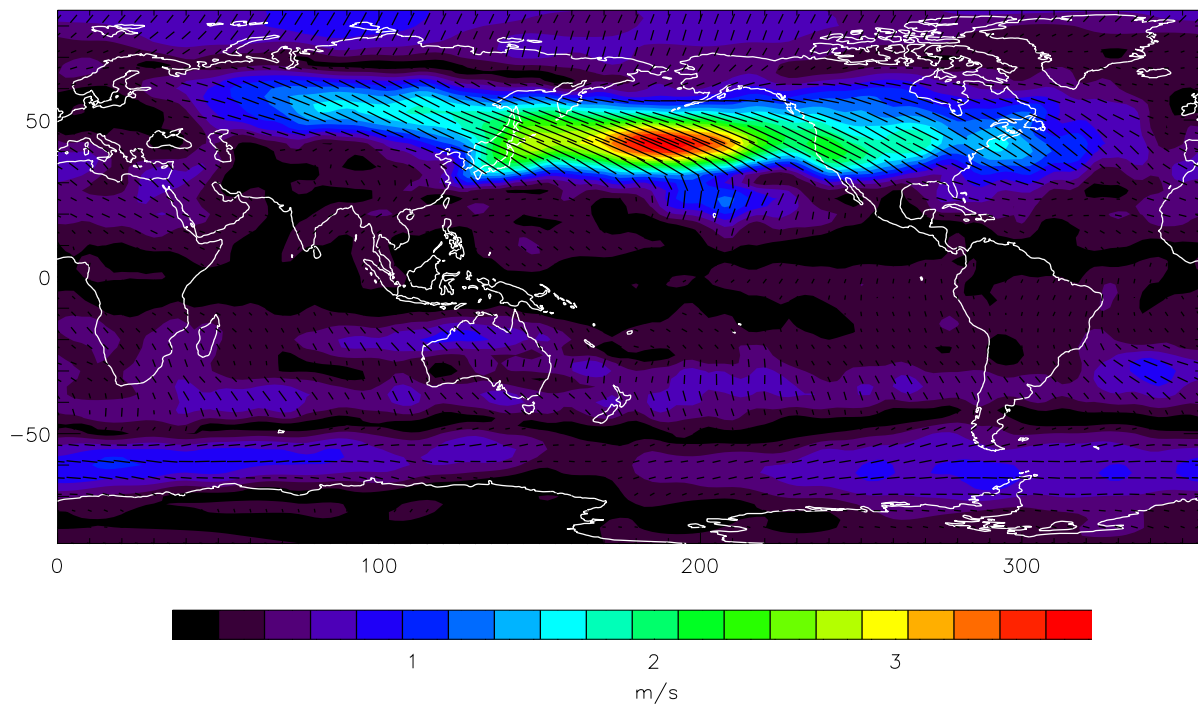


Figure 5: Semiannual harmonic of eddy activity (9-day running standard deviation of meridional wind) at 250 hPa. Colors and length of line segments indicates amplitude, while orientation indicates phase, with vertical indicating 1 Jan - 1 July and horizontal indicating 1 April - 1 October.

Figure 6 a,b

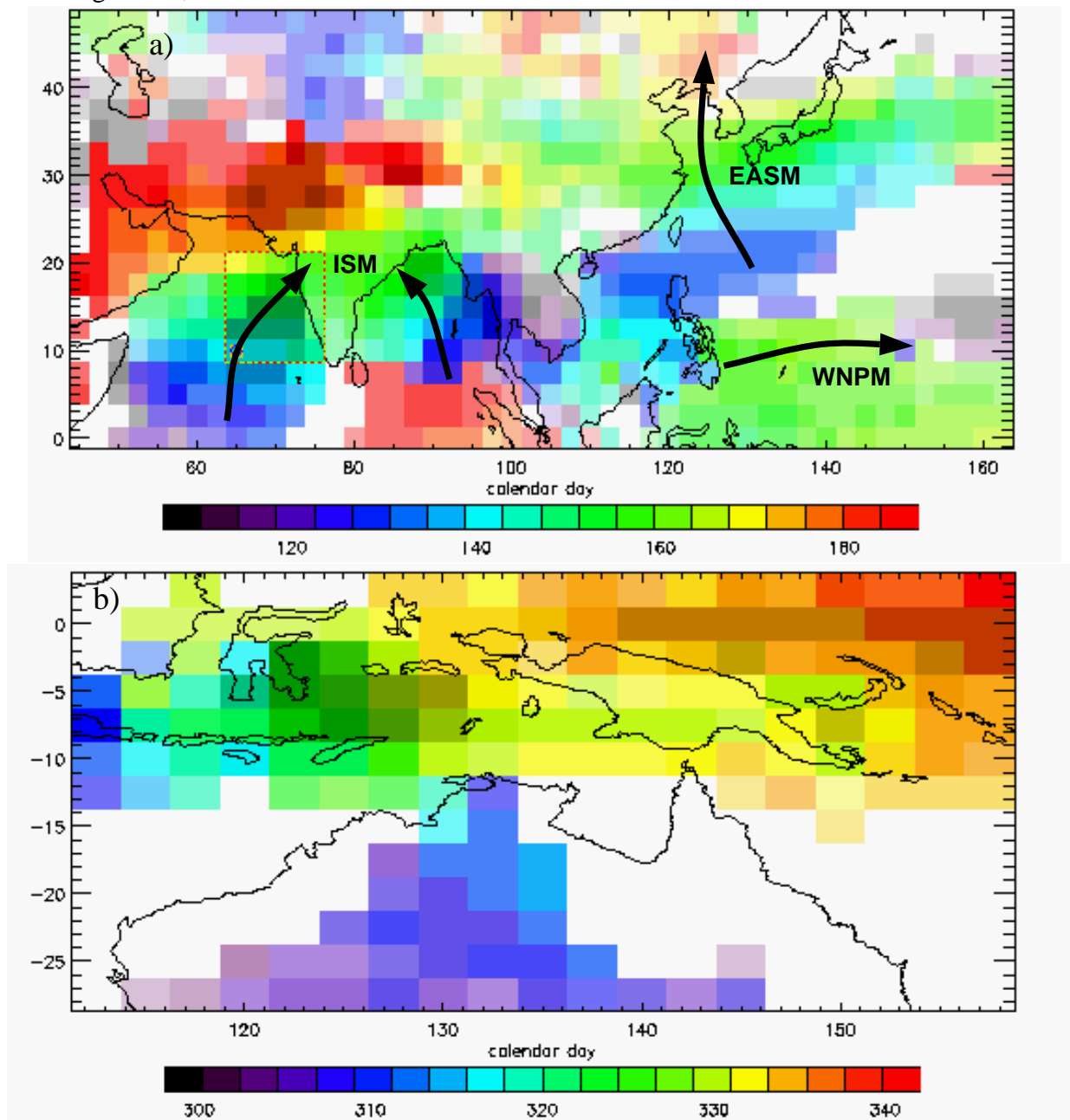


Figure 6c,d

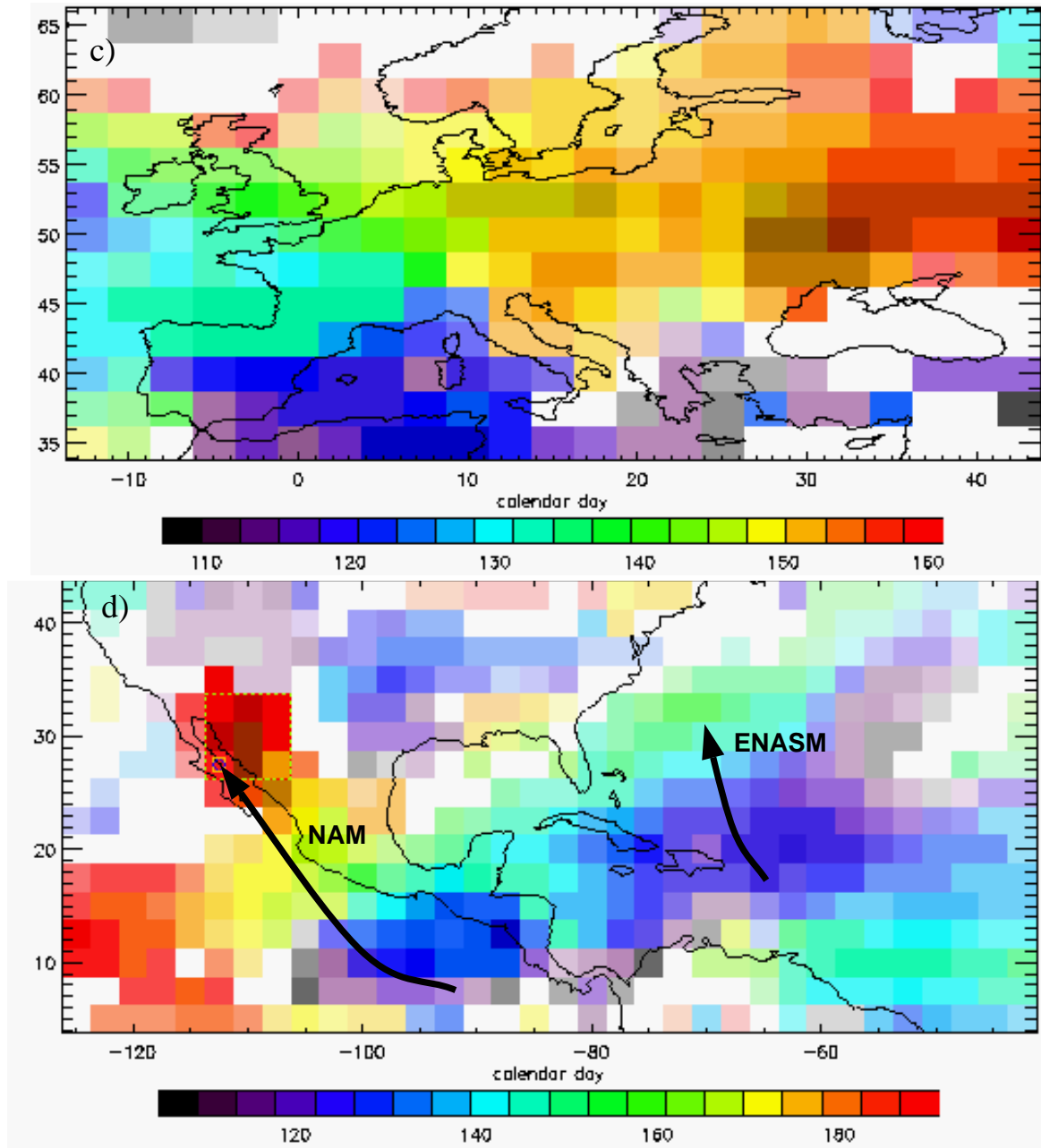


Figure 6: Onset dates, defined as the time of rapid increase in climatological mean summer monsoon cloudiness. At each gridpoint, the color is determined (according to the calendar-day color bar) by the date of the largest-amplitude wavelet imaginary power peak corresponding to a decrease in the local HF time series of OLR. The density of coloration is proportional to the peak's amplitude. If no power peak with significance index >0.8 exists within the time interval and within the wavelet-period range 25-140 days, the grid cell is left white. Annotations in a, d indicate coherent propagating onsets discussed in the text.

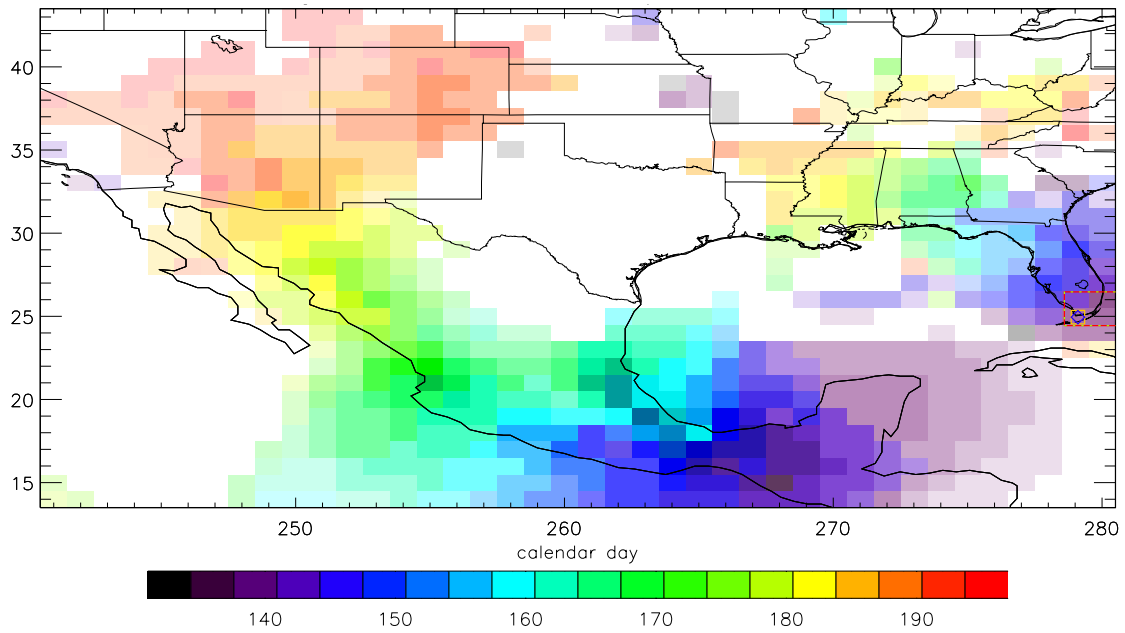


Figure 7: As in Fig. 6, but for onset defined as a HF rise in the time series of 1948-1998 mean rainfall in the gridded US-Mexico rain gauge analysis of Higgins et al. (2000). No rainfall data over water are used, so values there come purely from extrapolation in the gridding process.

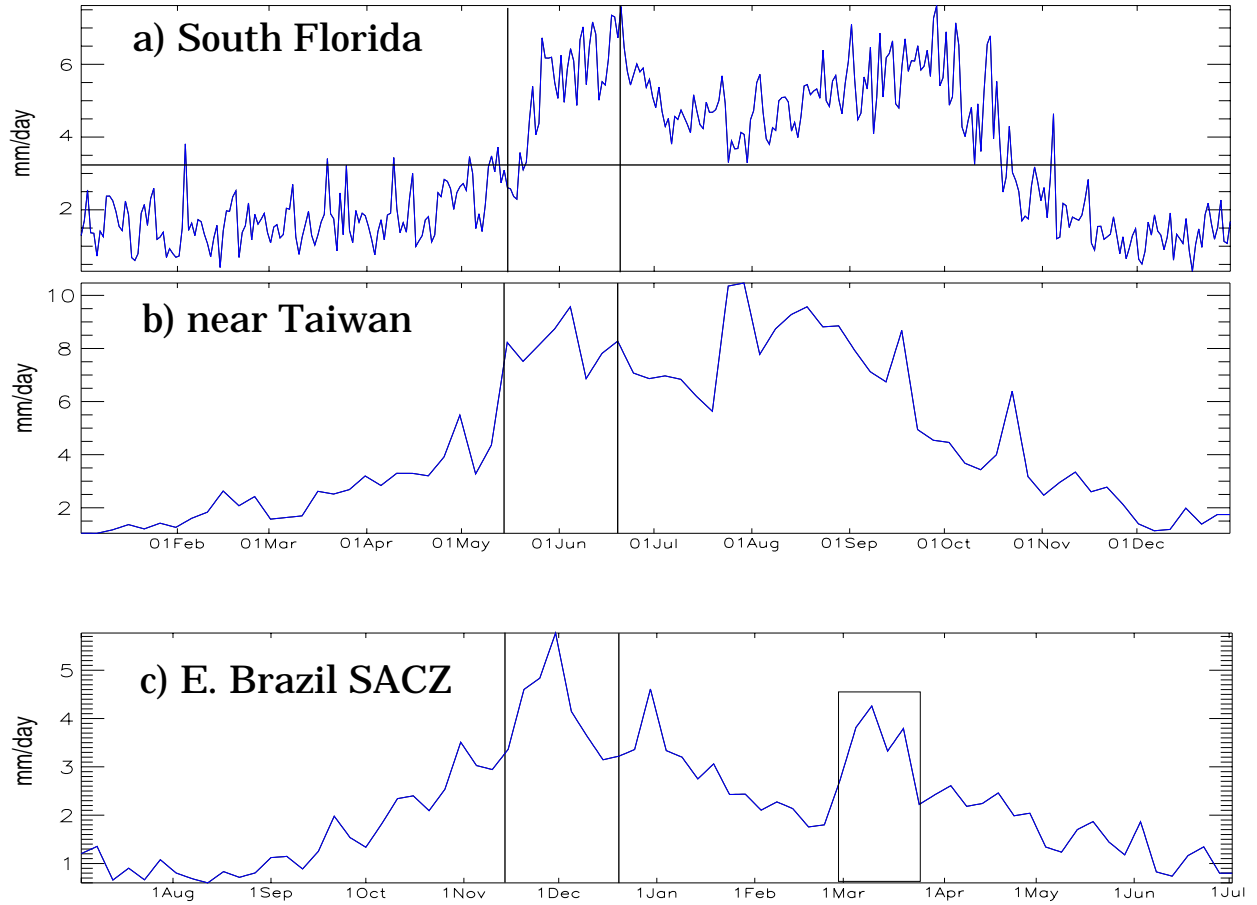


Figure 8: Climatological rainfall time series in three STCZ locations: a) South Florida, data from Higgins et al. (2002) climatology in the region indicated on Fig. 7; b) a region near Taiwan, CMAP data at pentad resolution; c) eastern Brazil and adjacent waters (box indicated on Fig. 11), CMAP pentad data.

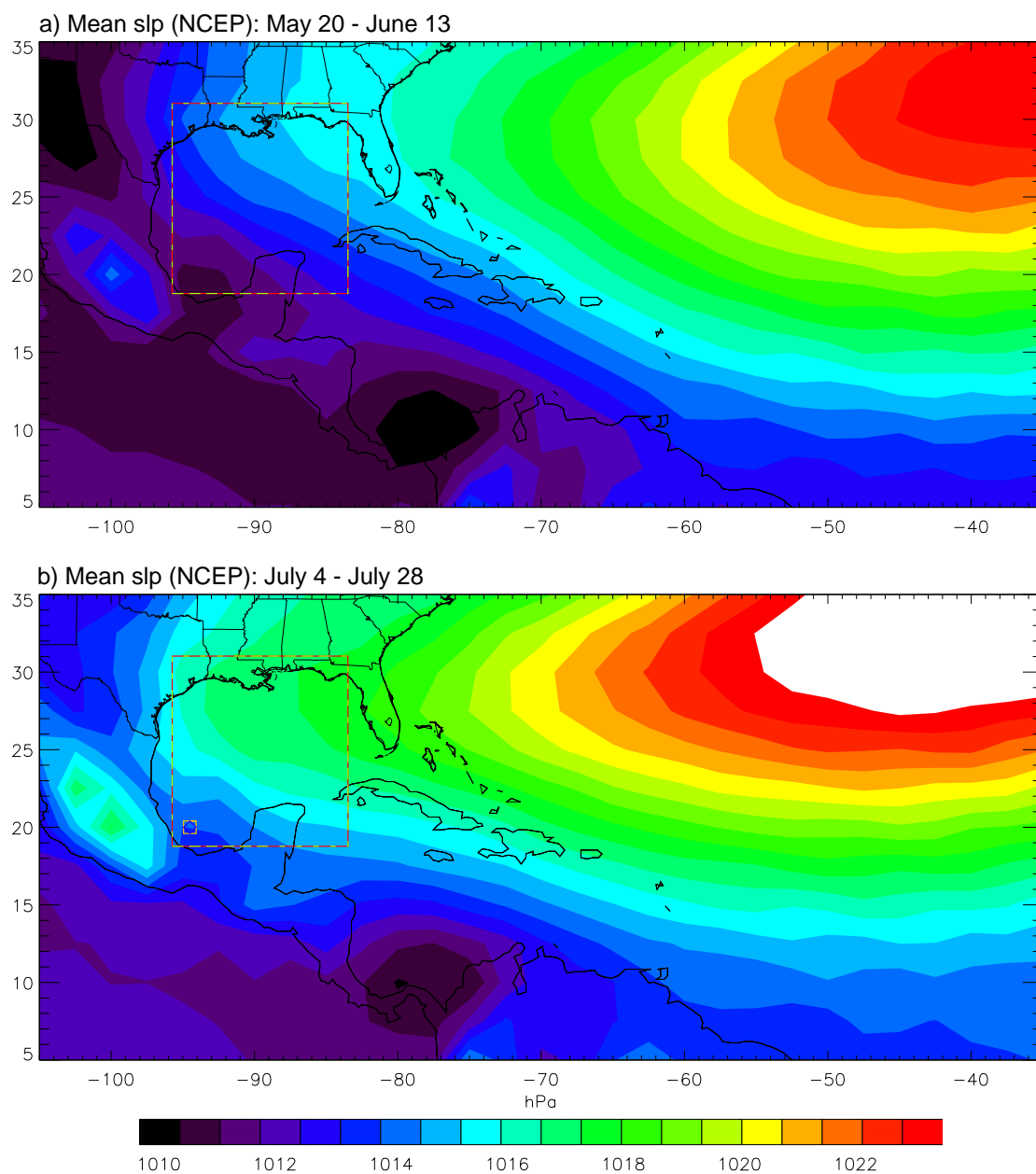


Figure 9: Sea level pressure in early summer and middle summer, from NCEP/NCAR reanalysis climatology. White areas have SLP off the red end of the color scale.

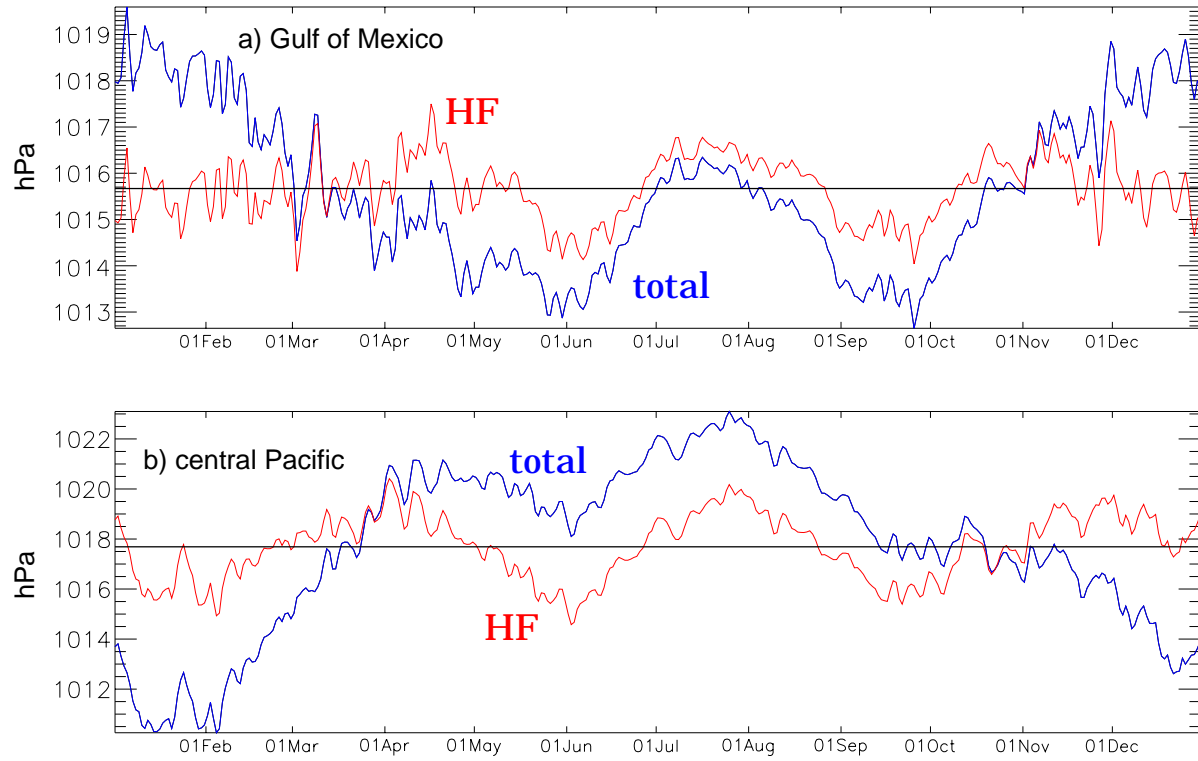


Figure 10: Reanalysis climatological SLP time series, total (blue) and high frequency (HF) components (red), for a) the Gulf of Mexico box indicated on Fig. 9; and b) a large box in the central North Pacific.

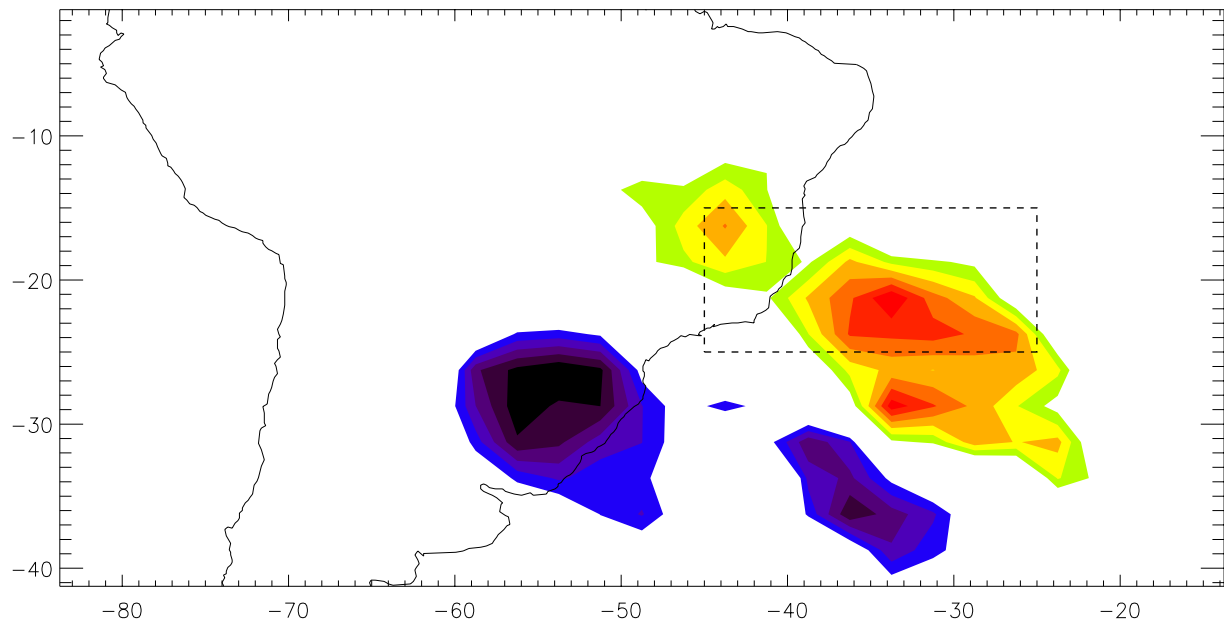


Figure 11: Contour map of the HF anomaly of CMAP rainfall during March (specifically, the time period boxed on Fig. 8c). Green-red colors indicate positive anomalies 0.5-1.5 mm/d, while blue-black anomalies denote negative anomalies -0.5 to -1.5 mm/d.

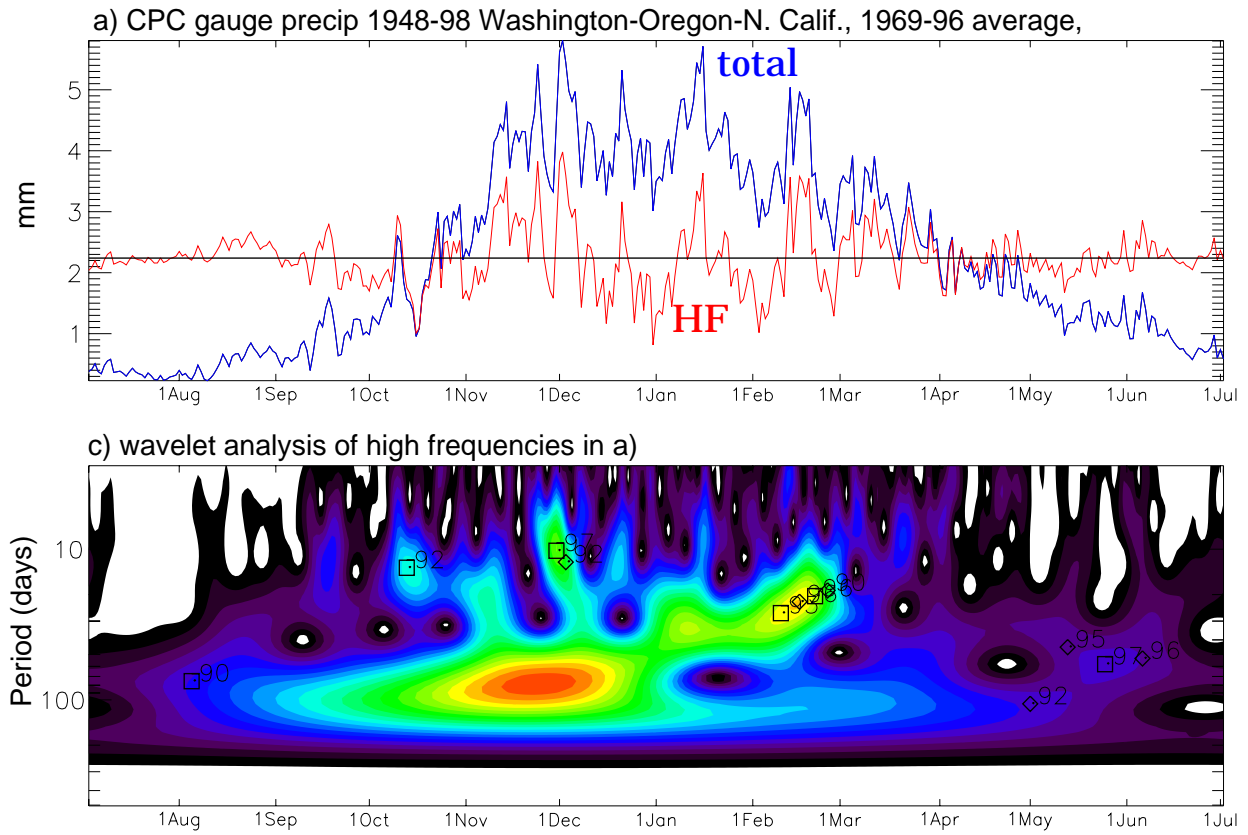


Figure 12: a) Total (blue) and HF (red) time series of gauge precipitation analysis for a U.S. Pacific Northwest region covering Washington, Oregon, and northern California. b) As in a), but for zonal wind at 500 hPa. c) Wavelet analysis with conventions as in Fig. 2 of the HF time series in a). d) As in c), but for the HF time series in b).

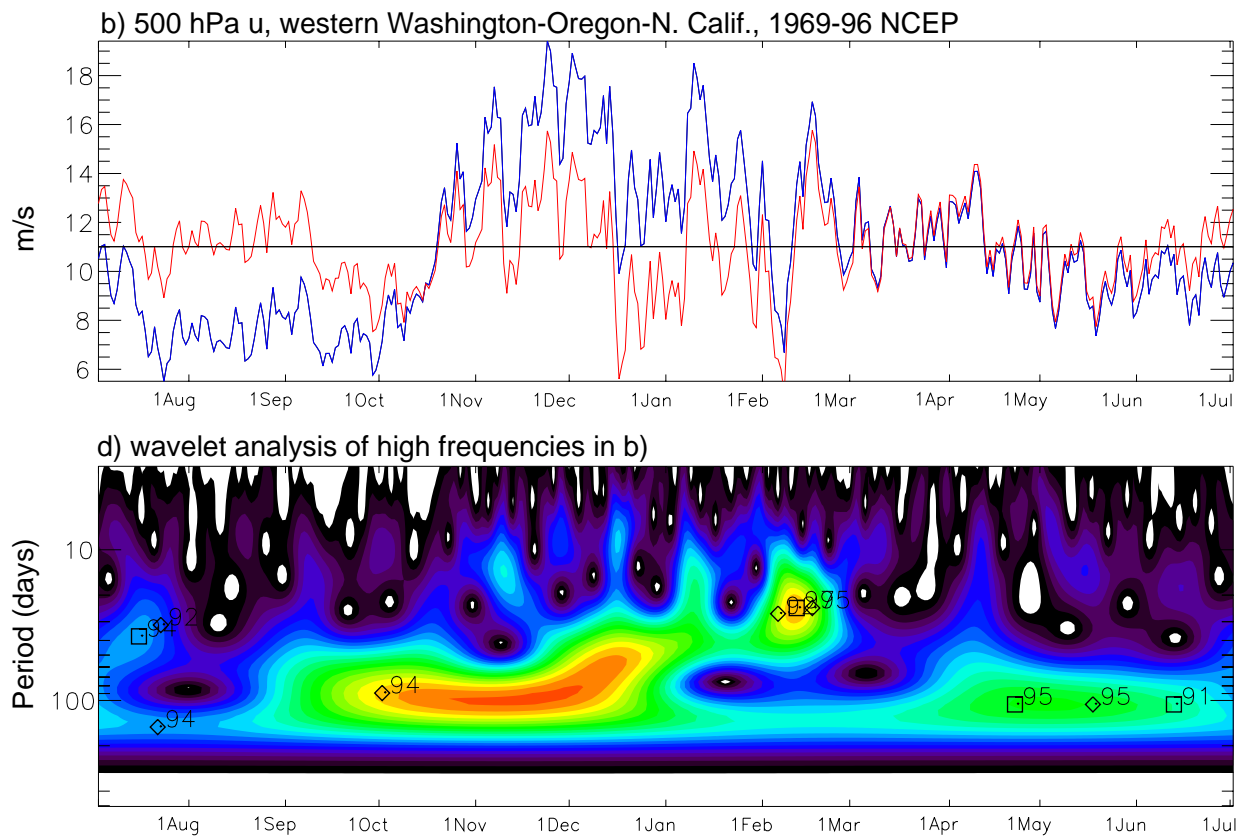


Figure 12, continued

